

# Prediction of Radio Wave Propagation Loss in ultra-Rugged Terrain Areas

Huafu Li, Wenzhe He, and Xianguo He

**Abstract**—When designing and maintaining a wireless network, engineers need to first evaluate the impact of a specific propagation environment on radio wave propagation. Currently, although many popular propagation models (PMs) are available for reference, their analysis and validation in ultra-rugged terrain areas (uRTAs) are still underexplored. This paper aims to implement an uRTA propagation model (uRTAPM), which consists of two modes, i.e., the point-to-point (uRTAPM-P2P) and the point-to-area (uRTAPM-P2A) modes, to meet the requirements of practical applications. First, we consider digital elevation model (DEM) data sets and three types of propagation, i.e., line of sight (LOS), non-LOS (NLOS), and multi-obstacle propagation. Second, we propose a cone multi-path model to simulate the NLOS diffraction behavior caused by mountains. Third, we utilize a triangulated irregular network (TIN) to finely divide the terrestrial surface of uRTAs. Finally, based on numerical calculations, compared with the existing commonly used PMs, the uRTAPM is found to reveal more details about the propagation loss (PL) caused by the terrain in uRTAs. The measurements demonstrate that the mean absolute error (MAE), root mean square error (RMSE), and standard deviation (SD) between the uRTAPM predicted values and the actual measured values are lower than those of other methods.

**Index Terms**—Wireless communication, propagation model, propagation loss prediction, ultra-rugged terrain areas.

## I. INTRODUCTION

THE wireless channel is one of the main factors affecting the performance of wireless communication systems. This factor determines whether a wireless signal can be reliably transmitted from the transmitting antenna to the receiving antenna. The radio wave propagation model (PM) in a specific propagation environment is directly related to the selection of the communication equipment, the determination of the antenna height, the estimation of the propagation distance, and a series of technical measures adopted to achieve a highly robust wireless communication system in engineering design [1], [2]. Next-generation mobile communication systems and vehicle networking technologies used in real-world scenarios cannot readily replicate the transmission effects achieved in the laboratory. The key reason is that the complex topography [3] and changeable meteorological conditions [4] in the real environment lead to considerable fading in radio waves, and the investigation and verification of fading in ultra-rugged terrain areas (uRTAs) have been insufficient.

This work was supported by the National Natural Science Foundation of China (No. 61841113). (Corresponding author: Wenzhe He.)

Huafu Li and Wenzhe He are with the School of Physics and Electronic Information, Yunnan Normal University, Kunming 650500, China (e-mail: Fairme@163.com; wendell31132@hotmail.com).

Xianguo He is with the Baoshan Branch, China Mobile Group Yunnan Co., Ltd., Baoshan 678000, China (e-mail: hexianguo.bs@yn.chinamobile.com).

In this research, an uRTA is defined as a mountainous area with  $\Delta h > 1000$  m. Roughly speaking, the  $\Delta h$  is the interdecile range of terrain elevations, that is, the total range of elevations after the highest 10% and the lowest 10% have been removed; the terrain types and  $\Delta h$  values are shown in Table I [5]. The parameter  $\Delta h$  of the research area studied in this paper exceeds 1000 m, which is not within the scope of Table I. Currently, to fully cover tourist attractions, villages, highways, and cultivated land in mountainous areas, China's telecom operators have made many efforts to effectively locate base stations (BSs) and select equipment. However, the quality of service (QoS) is often unsatisfactory mainly because the crisscrossing mountains, disorganized vegetation, and changeable atmosphere in this area provide scattering obstacles of the same magnitude as the wavelength, thereby increasing the uncertainty of radio wave attenuation and affecting the performance of wireless communication systems in unexpected ways.

In the past few decades, many researchers have paid close attention to PMs for predicting propagation loss (PL) in irregular terrains [6]–[9]. Empirical models include the Okumura-Hata model [10], COST-231 model [11], and standard propagation model (SPM) [12]. In fact, these PMs are all derived from the model developed by Okumura *et al.* [10]; this model estimates the general terrain knowledge involved. These PMs use the method of regional equivalent average to equate mountainous terrain to quasi-smooth terrain. Comparatively speaking, some irregular terrain PMs, such as Bullington's method [13] and Epstein-Petersen's method [14], idealize the mountain as a knife-edge model. Bullington's method replaces multiple obstacles with a single "equivalent" obstacle. This equivalent obstacle is then determined by the intersection of the steepest transmitter tangent and the steepest receiver tangent, and the diffraction loss is calculated using the Fresnel principle. However, most of the physically existing obstacles do not impact the locations of the equivalent obstacles, and this equivalence is considerably inaccurate. Epstein-Petersen's method calculates the loss of a specific obstacle by placing virtual "transmitters" and "receivers" on top of adjacent obstacles and then superimposes the attenuation of different obstacles. As a result, Epstein-Petersen's method of separately calculating the diffraction loss of each obstacle optimizes Bullington's method of using only two obstacles to determine the equivalent obstacles and improves prediction accuracy. In addition, the PM, which considers the terrain details and can be used for engineering applications, was first proposed by Longley *et al.* [5], and is called the Longley-Rice model. The model predicts the PL in different types of terrain

through extensive field measurements combined with the path geometry of topography and the diffraction principle of the troposphere. The Institute for Telecommunications Sciences (ITS), a research and engineering laboratory of the National Telecommunications and Information Administration (NTIA) in the United States, developed the irregular terrain model (ITM), also known as the ITM-LongleyRice model [15]. Until recently, the ITM-LongleyRice model was a baseline model for predicting the field strength of irregular terrains [15], [16]. Similar to the ITM-LongleyRice model, the Durkin model was proposed by Edwards, Durkin, and Dadson *et al.* [17]. Compared with the ITM-LongleyRice model, the Durkin model is claimed to be able to calculate more complicated diffractions with two and three obstacles. However, the ITM-LongleyRice model and the Durkin model are modeled only by the single-path diffraction of obstacles along the  $L-O-S^1$  without considering the effects of multi-path propagation and local scattering; the result is some pessimism in predicting complex terrains (especially canyon terrains, where the slope drops rapidly). Some researchers consider the influence of multi-path propagation of obstacles with limited width and model both sides of the stripe [18] or human body [19]–[21] as knife-edge models to estimate the degree of the obstacles's resistance to electromagnetic waves. However, no study of an equivalent mountain as an obstacle with a finite width has been conducted, and the traditional method equates a mountain only to a knife-edge model with an infinite width to simplify calculation. To improve the efficiency of network planning and network optimization in uRTAs, an accurate PL estimation method needs to be accompanied by more discussion, analysis, and justification.

In recent years, few studies have been published on PL prediction and wireless channel measurement in mountainous areas mainly due to the number of users and the demand for wireless signal quality; researchers and operators have paid more attention to the deployment and optimization of wireless networks in urban environments [22]–[24]. Compared with human factors, such as buildings, the terrain influences the urban wireless environment much less. In addition, research on indoor scenes and millimeter wave technology has received broad attention [25]–[28], and compared to other directions, these research directions seem to more easily meet the needs of data traffic. To the best knowledge of the authors, the most relevant progress in predicting PL in rugged terrain includes the optimization and improvement of some classic models (e.g., the two-ray model and the knife-edge diffraction model [29]), the correction of existing model parameters by test data [10], and the enhancement of adaptation to specific environments (e.g., forest terrains [30] and hilly islands along sea/ocean paths [31]). However, with the withdrawal of 2G/3G networks, operators are considering recultivating 5G networks in low frequency bands (e.g., 900 MHz). Compared to millimeter waves, low frequency bands are very suitable for the breadth and depth coverage of rugged terrains. In

<sup>1</sup>Throughout the text, LOS (line of sight)/NLOS (non-LOS) refers to a propagation phenomenon without/with obstacles between transceivers, but  $L-O-S$  refers to the connection line between transceivers, such as the  $TR$  line segment in Fig. 2.

Table I  
SUGGESTED VALUES FOR THE TERRAIN IRREGULARITY PARAMETER

Terrain type	$\Delta h$ (meters)	Terrain type	$\Delta h$ (meters)
Flat / smooth water	0	Plains	30
Hills	90	Mountains	200
Rugged mountains	500		

the future, with the growing maturity of mountain tourism, intelligent monitoring, automatic driving and the Internet of things technologies, the value of how to effectively improve the quality of wireless network coverage in mountain areas and further achieve refined network planning and network optimization will become increasingly apparent.

This paper focuses on the propagation environment of uRTAs (i) to implement a highly accurate point-to-point (P2P) field strength prediction method and to meet the needs of engineering applications and (ii) to use a triangulated irregular network (TIN) algorithm to finely dissect terrestrial surfaces and combine it with the P2P prediction method to calculate the PL from a specific point to a given area, i.e., the point-to-area (P2A) prediction method. Through the research of the PL in uRTAs, wireless system designers can set reasonable fading margins for new networks and provide substantive suggestions, such as equipment selection. In addition, to accurately evaluate adjacent frequency interference, adjacent cell interference, and channel time-varying state, the method in this paper can be used to predict the field strength coverage in the target area with the given transmitter parameters.

The rest of this paper is organized as follows. Section II starts from the data preparation and propagation principle and provides the implementation details of the uRTA propagation model (uRTAPM). Section III evaluates the feasibility and reliability of the uRTAPM by using simulations and actual measurements and compares the performance of the model with other popular PMs. Section IV discusses practical engineering problems, model optimization problems, simulation limitations, and future work prospects. Section V presents the conclusion.

## II. METHODOLOGY

Radio wave PL is related not only to the height of the base and mobile station, frequency, etc., but also to specific topography, ground cover, and the artificial environment. This section describes the implementation details of the method for predicting PL in uRTAs.

### A. DEM Data

The digital elevation model (DEM) data contain the mapping relationship between the plane coordinates ( $X, Y$ ) and the elevation  $Z$  in the relevant region, and these data are usually in the form of a discrete dataset with a distinct sampling precision, expressed as  $Z = F(X, Y)$ . In this paper, the 7.5-minute DEM data (30- by 30-meter data spacing, cast on the Universal Transverse Mercator projection) storage format is shown in Fig. 1. The DEM contains only terrain elevation values. The reflection and scattering loss caused

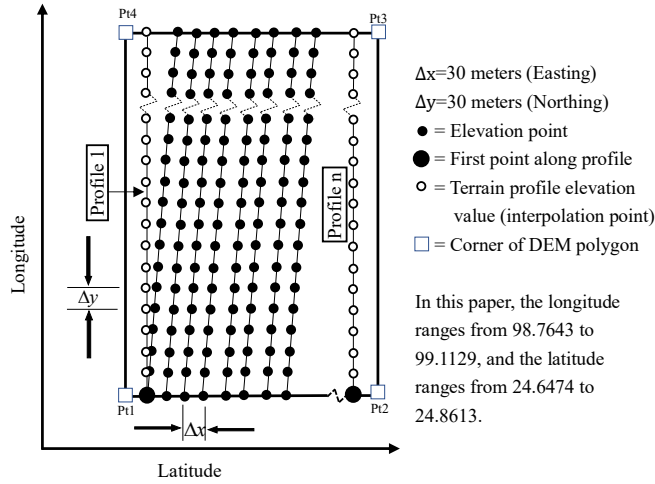


Fig. 1. DEM data storage diagram.

by surface vegetation or clutter are estimated by Longley-Rice's empirical data [5]. See Table II for the surface relative permittivity, surface conductivity, and surface refractivity.

### B. TIN Grid

To more accurately represent the real terrain by using DEM data, this paper uses the TIN algorithm [32] to finely divide terrestrial surfaces. The TIN-based method can change the density of sampling points and determine their location according to the fluctuation of the terrain; consequently, this method can not only avoid the problem of redundant data in areas with little terrain fluctuation and reduce computational complexity but also improve the simulation veracity with respect to topographic features, such as ridges, valleys, and terrain change lines. In [33], the TIN grid was found to be more accurate than the traditional quadrilateral grid in describing terrain information. The TIN dataset is a collection of three-dimensional (3D) coordinates associated with each DEM sampling point; these coordinates are connected by lines to form a triangle without overlap, as shown in Fig. 6.

### C. Propagation Theory

1) *Free-space Propagation Model:* This model describes the PL of the transceiver in a completely unobstructed LOS environment. The *PL* is used to represent the propagation loss value with a specific frequency; *PL* is defined as the difference between the effective transmit power and the received power and is expressed as

$$PL(dB) = 10 \lg \frac{P_t}{P_r} = -10 \lg \left[ \frac{G_t G_r \lambda^2}{(4\pi)^2 d^2} \right], \quad (1)$$

where  $P_t$  is the transmission power,  $P_r$  is the reception power,  $G_t$  is the transmission antenna gain,  $G_r$  is the reception antenna gain,  $\lambda$  is the signal wavelength in meters, and  $d$  is the distance between the antennas in meters.  $\lambda = c/f$ , where  $c$  is the speed of light, or  $3 \times 10^8$  m/s, and  $f$  is the frequency

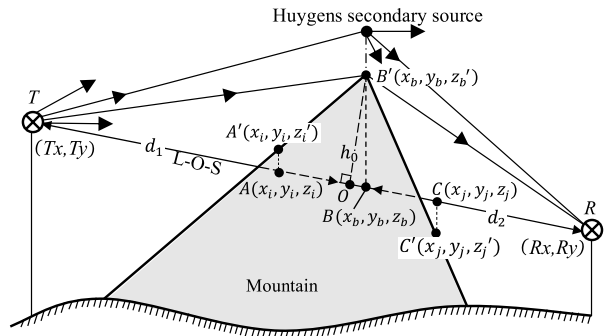


Fig. 2. Knife-edge diffraction model.

in Hz. The units of power and gain are W, and when they are converted to mW, the *PL* is expressed as

$$PL(dB) = 10(2 \lg f + 2 \lg d - \lg G_t - \lg G_r) - 147.56. \quad (2)$$

2) *Two-ray Ground Reflection Model:* In reality, single-path propagation under LOS is rare; the two-ray ground reflection model, which is based on geometric optics, has proven to be very accurate in predicting the cellular environment within several kilometers, and spatial diversity is often used to reduce interference. If  $d > 4h_t h_r / \lambda$  [34],  $P_r$  can be expressed as

$$P_r = P_t G_t G_r \frac{h_t^2 h_r^2}{d^4}, \quad (3)$$

where  $h_t$  is the height of the transmitter relative to the ground in meters and  $h_r$  is the height of the receiver relative to the ground in meters. When the units of  $P_r$ ,  $P_t$ ,  $G_t$ , and  $G_r$  are converted from W to mW, the *PL* is expressed as

$$PL(dB) = 40 \lg d - 10(\lg G_t + \lg G_r + 2 \lg h_t + 2 \lg h_r). \quad (4)$$

3) *Knife-edge Diffraction Model:* It is impossible to accurately predict the loss of radio waves caused by obstacles such as mountains and buildings, and the common method is to combine theoretical approximations with necessary corrections based on experience. The knife-edge diffraction model is often used to evaluate the attenuation of radio waves by obstacles, as shown in Fig. 2. According to Huygens's principle, all points on the diffracted wave front can be used as point sources for generating secondary waves, which combine to form a new wave front in the propagation direction. The total field strength  $E_{total}$  at any point in the shadow area is the vector sum of the field strength of all Huygens secondary sources on the knife-edge, and the diffraction gain  $G$  can be provided by the Fresnel integral; i.e.,

$$G = \frac{E_{total}}{E_0} = F(v) = \frac{(1+j)}{2} \int_v^\infty e^{-j\pi \frac{t^2}{2}} dt, \quad (5)$$

where  $E_0$  is the free-space field strength, and  $F(v)$  is the Fresnel number. If  $\angle OTB'$  and  $\angle ORB'$  are small, the Fresnel-Kirchhoff diffraction parameter  $v$  is estimated as

$$v \approx h_0 \sqrt{\frac{2}{\lambda} \left( \frac{1}{d_1} + \frac{1}{d_2} \right)}, \quad (6)$$

where  $h_0$  represents the diffraction clearance in meters and  $d_1$  and  $d_2$  are the distances in meters of the transmitter and

receiver, respectively, along the *L-O-S* to the obstacle. It is complicated to find the integral of Eq. (5), and Lee [35] provides an approximate solution as

$$\left\{ \begin{array}{l} G = 0, v \leq -1 \\ G = 20 \lg(0.5 - 0.6v), -1 < v \leq 0 \\ G = 20 \log(0.5 \exp(-0.95v)), 0 < v \leq 1 \\ G = 20 \log(0.4 - \sqrt{0.1 - (0.4 - 0.1v)^2}), 1 < v \leq 2.4 \\ G = 20 \log(0.23/v), v > 2.4 \end{array} \right. . \quad (7)$$

In Eqs. (5) and (6), the diffraction gain of the knife-edge is related only to  $v$ , which is related to  $h_0$ ,  $d_1$ ,  $d_2$ , and  $\lambda$ .

#### D. uRTAPM Algorithm

This section introduces a model that predicts PL in uRTAs. (i) The transceiver coordinates are known, and (ii) when modeling,  $P(x, y)$  means that the longitude and latitude coordinates of point  $P$  have been projected as geodetic plane coordinates.

**1) Calculate Terrain Profile Data:** The terrain profile of any propagation path is reconstructed. Considering that the *L-O-S* sampling points do not necessarily coincide with DEM sampling points, the elevation values of any sampling points on the *L-O-S* are obtained by bilinear interpolation. Fig. 3 (a) shows a top view of the sampled DEM data, and Fig. 3 (b) shows the reconstructed terrain profile. In the projection coordinate system, the elevation values of the four points attached to point  $P(x, y)$  are expressed as  $Q_1(x_1, y_1)$ ,  $Q_2(x_2, y_1)$ ,  $Q_3(x_2, y_2)$ , and  $Q_4(x_1, y_2)$ ; in addition,  $R_1(x, y_1)$  and  $R_2(x, y_2)$  are intermediate variables. According to Eq. (8), the elevation value of point  $P$  can be obtained.

$$\left\{ \begin{array}{l} R_1 = \chi Q_1 + \alpha Q_2 \\ R_2 = \chi Q_4 + \alpha Q_3 \\ P = \phi R_1 + \beta R_2 \\ P = \chi \phi Q_1 + \alpha \phi Q_2 + \beta \chi Q_4 + \alpha \beta Q_3 \end{array} \right. , \quad (8)$$

where  $\chi = (1 - \alpha)$ ;  $\phi = (1 - \beta)$ ;  $\alpha = (x - x_1)/(x_2 - x_1)$ ;  $\beta = (y - y_2)/(y_1 - y_2)$ ; and  $R_1$ ,  $R_2$ ,  $Q_1$ ,  $Q_2$ ,  $Q_3$ ,  $Q_4$ , and  $P$  are the elevation values of the corresponding coordinates. In Fig. 3 (a),  $A$ ,  $P$ , and  $B$  are equidistant sampling points on the *L-O-S*, and the elevation values of these points are calculated by Eq. (8); the elevation values are expressed as  $\mathbf{H} = [H_A, H_P, H_B]$ , and the distance matrix is expressed as  $\mathbf{D} = [D_A, D_P, D_B]$ . From  $\mathbf{H}$  and  $\mathbf{D}$ , the difference between the actual elevation of each sampling point and the *L-O-S* is calculated as  $h_A$ ,  $h_P$ , and  $h_B$  in Fig. 3 (b), where if  $h_A > 0$ , point  $A$  is above the *L-O-S*, and if  $h_P < 0$ , point  $P$  is below the *L-O-S*.

**2) Calculate the Number of Mountains:** The algorithm for calculating the number of mountains between transceivers is as follows.

**Step 1:** As shown in Fig. 2, starting from the transmitter, samples with equal distances (30 m) along the *L-O-S* are denoted as  $(x_i, y_i, z_i) \{i = 1, 2, 3, \dots, n\}$ .  $A$ ,  $B$ , and  $C$  are the sampling point elevations on the *L-O-S*, and  $A'$ ,  $B'$ , and  $C'$  are the corresponding real elevations on the mountain.

**Step 2:** When the real elevation value of the  $i$ -th sampling point is greater than the value of the point on the *L-O-S*, that

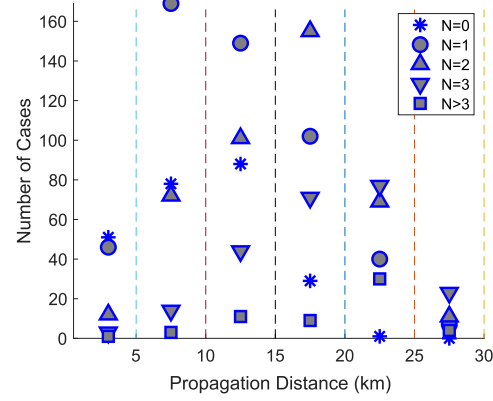


Fig. 4. Statistics on the number of mountains ( $N$ ) in the target area (longitude: 98.7643 to 99.1129, latitude: 24.6474 to 24.8613). The x-coordinate is the P2P propagation distance, and the y-coordinate is the number of cases that satisfy the corresponding  $N$ .

is,  $z'_i - z_i \geq 0$ , it is calculated whether the next sampling point still satisfies this condition; i.e., if  $z'_{i+1} - z_{i+1} \geq 0$ , then point  $A(x_i, y_i, z_i)$  is the first intersection point between the *L-O-S* and the mountain body. We record the coordinates and subscript of this point and set  $Flag = 1$  to enable the valid intersection point variable. If  $z'_{i+1} - z_{i+1} \leq 0$ , point  $A(x_i, y_i, z_i)$  is tangent to the mountain; record the coordinates and subscript of this point and set  $Flag = 0$  to indicate that the intersection variable is invalid.

**Step 3:** If  $Flag = 1$ , until  $z_j - z'_j \geq 0$  and the  $j$ -th sampling point is the second intersection point between the *L-O-S* and the mountain, record these point coordinates  $(x_j, y_j, z_j)$ . The number of mountains is stored in variable  $N$ , and  $N = N + 1$ . Setting  $Flag = 0$  means that one mountain body has been identified.

**Step 4:** Calculate the maximum elevation value of the sampling point subscript from  $i$  to  $j$ ; this value is denoted as  $B'(x_b, y_b, z'_b)$ . Then, return to **Step 2** until all sampling points on the *L-O-S* are calculated.

**Step 5:** When **Step 2** ends, if  $Flag = 0$ , return to **Step 2** until all sampling points on the *L-O-S* are calculated.

The number of mountains is evaluated by  $N$  in **Step 3**.  $N=0$  indicates that there are no mountains between transceivers,  $N=1$  indicates that there is one mountain between transceivers,  $N=2$  indicates that there are two mountains between transceivers, and so on.

Based on the above algorithm, MATLAB is used to calculate the statistical results of the propagation distance and the number of mountains in the target area when the transmitter coordinates (24.7153, 98.8834) are fixed and 1470 receiving virtual points are selected on average, as shown in Fig. 4. The results show that when the propagation distance is in the range of 0~5 km,  $N=0$  (no mountain) is the most common result, followed by  $N=1$  (there is one mountain); when the propagation distance is in the range of 5~10 km,  $N=1$  is the most common result, followed by  $N=0$ , and so on.

**3) Calculate the Propagation Type:** According to Sections II-D1 and II-D2, as shown in Fig. 2, if  $N = 1$ , the diffraction clearance  $h_0$ , the point  $O$  coordinates, and  $d_1$  and  $d_2$  are

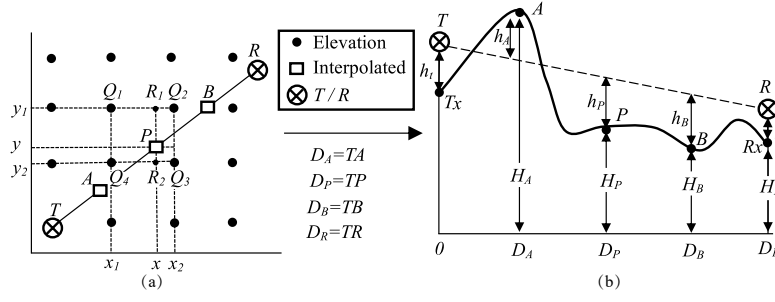


Fig. 3. Terrain data processing method. (a) DEM data sampling points and interpolation diagram. (b) Reconstruction of terrain profile.

calculated by using the DEM data. Then, the coefficient  $v$  is calculated by Eq. (6). Based on this, the following propagation types are considered. (i)  $v \leq -0.8$ , which corresponds to LOS propagation with sufficient Fresnel clearance (i.e., the first Fresnel zone), where the PL can be calculated by the free-space model, i.e., Eq. (2). (ii)  $-0.8 < v < 0$ , which denotes LOS propagation but not sufficient Fresnel clearance, where the PL can be calculated by the two-ray ground reflection model, i.e., Eq. (4). (iii)  $v = 0$ , where the L-O-S is tangent to the mountain (see Section II-D2, Step 2), and the PL is the free-space loss minus 6 dB. (iv)  $v > 0$ , which indicates NLOS propagation, where the PL needs to increase the Fresnel diffraction gain according to Eq. (7). If  $N = 2$ ,  $N = 3$ , or  $N > 3$ , see Section II-D4.

4) *NLOS Propagation*: In this research, three kinds of NLOS diffraction propagation are considered, i.e., one mountain, two mountains, and three mountains. If  $N = 2$  or  $N = 3$ , the method of Epstein-Peterson [34] is used to approximate the multi-mountain diffraction loss. In short, to calculate the attenuation of a particular mountain, the virtual “transmitter” and “receiver” are placed on its left and right, respectively, and the complex multi-mountain diffraction is simplified into single-mountain diffraction. Then, the diffraction coefficient can be calculated as instructed in Section II-D3. Finally, the loss gains caused by different mountains are superimposed on the free-space loss to obtain the total attenuation at the receiver. When  $N > 3$ , although the diffraction calculation can also be performed by the aforementioned method, the result is a sharp rise in computational complexity. Therefore, this paper uses the  $\Delta h$  from the Longley-Rice model [5] to estimate this type of PL. However, with the development of wireless communication systems, to improve the speed and throughput, the coverage area is decreasing, and it is rare for the region between the transceivers to have more than three mountains, as shown in Fig. 4.

5) *Multi-path Propagation*: Simplifying the mountain-to-knife-edge model is considered a common and effective approach. However, this approach is not perfect in reality mainly because this assumption regards only the peak position as a Huygens secondary source and ignores the influence of the bulge on the attenuation of radio waves on both sides of the mountain. Neither the Longley-Rice model nor the Durkin model considers this multi-path propagation. This section shows how the diffraction point is determined and calculated on both sides of the mountain.

This research extends the traditional knife-edge model to the cone hypothesis, which extends the 2D model to the 3D model. Compared with the traditional knife-edge model, the significance of the cone hypothesis in this paper is that the mountain is equivalent to a limited-width obstacle composed of three knife-edge models; i.e., electromagnetic waves diffract not only from the top of the mountain but also from both sides of the mountain. In particular, in this paper, 2D refers to a mountain that is equivalent to a knife-edge model, which considers only the plane formed by the L-O-S direction of the transceiver and the effective diffraction clearance of the mountain, i.e., plane  $TR \perp h_0$ , as shown in Fig. 2. However, 3D means that the cone model should consider not only the effective height but also the effective width of the mountain, i.e., space  $h_0 \perp \overline{TR}$ ,  $h_1 \perp \overline{TR}$ , and  $h_3 \perp \overline{TR}$ , as shown in Fig. 5 (a). In Fig. 5 (a), considering the three-path propagation scenario caused by mountains between transceivers, the first path is a common knife-edge model, which is visually expressed as the diffraction propagation from the top of the mountain. The second and third paths are the paths of diffraction propagation from both sides of the mountain.

The most important aspect of the cone multi-path model is to calculate the diffraction clearance, that is, the distance from the Huygens secondary source to the L-O-S, which is shown as  $h_0$ ,  $h_1$ , and  $h_2$  in Fig. 5 (a). Since the first path can obtain altitude coordinates through sampling points,  $h_0$  is calculated as described in Section II-D3. For the second and third paths, we suppose that the angle between the L-O-S and east directions is  $\theta$  (calculated by the transceiver coordinates; this parameter is used to determine the sampling direction in the cone model) and set up the L-O-S  $\perp z$  coordinate plane with  $T$  as the origin. The calculation steps for the Huygens secondary source plane coordinate  $(x_k, y_k)$  of the second path when there is only one mountain between the transceivers are given as follows.

**Step 1:** The sampling coordinates on the L-O-S are denoted as  $(x_i, y_i, z_i)$ ,  $\{i = 1, 2, 3...n\}$ . As shown in Fig. 5,  $A(x_1, y_1, z_1)$ ,  $B(x_2, y_2, z_2)$ ,  $C(x_3, y_3, z_3)$ ,  $D(x_4, y_4, z_4)$ ,  $E(x_5, y_5, z_5)$ , and  $F(x_6, y_6, z_6)$ .

**Step 2:** For the  $i$ -th sampling point on the L-O-S, the sampling is carried out according to the  $z$  direction, and the sampling interval is  $\Delta d$  (30 m). In Fig. 5 (b), for example, the  $P$  point coordinates are expressed as  $(x_j, y_j, z_i)$ ,  $\{i = 1\}$  and are calculated by known coordinates as  $(j\Delta d \sin \theta + x_i, y_i - j\Delta d \cos \theta, z_i)$ ,  $\{i = 1, j = 1\}$ . Set  $i = i + 1$  and  $j = j + 1$  to

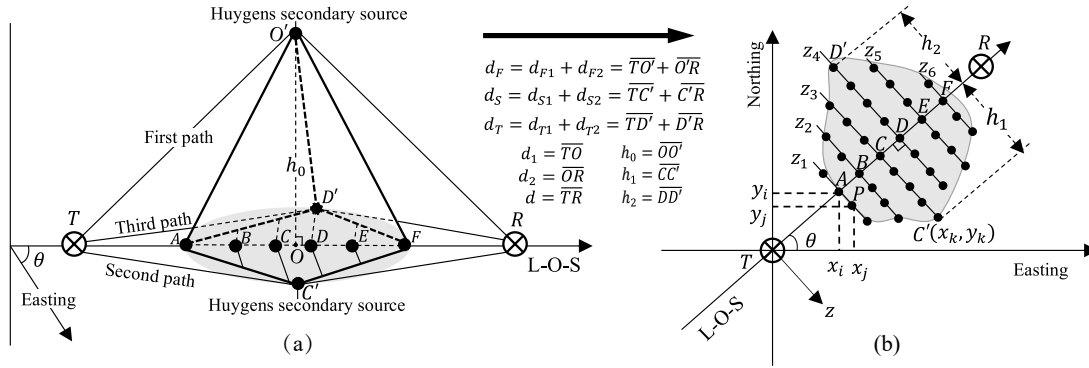


Fig. 5. Cone multi-path model. (a) 3D view. (b)  $L\text{-}O\text{-}S \perp z$  plane view.

traverse the sample points from the  $L\text{-}O\text{-}S$  and  $z$  directions, respectively.

**Step 3:** Determine the boundary conditions in the  $z$  direction. Taking the  $z_1$  elevation line as an example, when the real elevation value of the sampling point is less than  $z_1$ , this sampling point is the intersection point of the  $z_1$  elevation line and mountain.

**Step 4:** Repeat **Steps 2** and **3** for all sampling points on the  $L\text{-}O\text{-}S$  and  $z$  directions; calculate  $j\Delta d$  for each sampling point  $i$ ; and record  $k = j, n = i$ . That is, the point  $(x_k, y_k, z_n)$  (e.g.,  $n = 3$  in Fig. 5 (b)) has the largest vertical distance from the  $L\text{-}O\text{-}S$ ; this point is the Huygens secondary source coordinate of the second path, and the diffraction clearance  $h_1 = k\Delta d$ . The same method calculates  $h_2$ , in which case only  $z$  needs to be sampled in the reverse direction.

Finally, we can calculate the diffraction loss of each knife-edge diffraction model. See Annex A. According to the definitions of Fresnel zone geometry and the knife-edge diffraction model, each diffraction edge produces a statistically constant diffraction loss in a time-invariant flat fading environment. The total diffraction gain can be obtained by summing up three diffracted waves as follows [14], [20], [21], [36], [37]:

$$G_{total}(dB) = \sum_{i=0}^2 G\{v(h_i)\}. \quad (9)$$

**6) Calculation Process:** As stated previously, the prediction of uRTA PL is implemented. The P2P calculation of the uRTAPM is implemented by Algorithm 1 uRTAPM-P2P. The PL coverage prediction of the target region with the TIN grid is implemented by Algorithm 2 uRTAPM-P2A. The parameters mentioned in Algorithms 1 and 2 are described in Table II. Here,  $timepct$  represents the variation degree of the median attenuation caused by the air refractive index, air vibration, etc., within a unit time (one hour). In addition,  $locpct$  describes the statistical characteristics of differences caused by the ground or the environment. Furthermore,  $conpct$  includes some differences caused by other factors under the same system and environmental parameters, such as accuracy errors when manually reading the test values. Other specifications of parameters can be found in [5].

### Algorithm 1 uRTAPM-P2P

---

**Input:**  $ter_{pa}, pro_{pa}, sig_{pa}, env_{pa}, con_{pa}$ ;  
**Output:** P2P PL  $PL_{P2P}$ .

- 1:  $ter_{pa}$  includes DEM data, and transceiver coordinates.;
- 2:  $pro_{pa}$  includes  $h_r, h_t$ ;
- 3:  $sig_{pa}$  includes  $f$ , polarization mode;
- 4:  $env_{pa}$  includes surface refractivity, surface relative permittivity, and surface conductivity;
- 5:  $con_{pa}$  includes  $timepct$ ,  $locpct$ , and  $conpct$ ;
- 6: Prepare or transfer parameters for  $PL_{prop}$  function;
- 7: Implement arbitrary point interpolation function and calculate  $\mathbf{H}$  and  $\mathbf{D}$  matrices by Section II-D1.
- 8: **function**  $PL_{prop}$
- 9:   Check parameter ranges;
- 10:   Calculate propagation type (LOS/NLOS) by Section II-D3;
- 11:   **if** LOS **then**
- 12:     Prepare initial LOS constants;
- 13:     Calculate LOS coefficients and loss by Section II-D3;
- 14:   **end if**
- 15:   **if** NLOS **then**
- 16:     Prepare initial NLOS constants;
- 17:     Calculate the number of mountains  $N$  by Section II-D2;
- 18:     **if**  $N = 1$  **then**
- 19:       Calculate multi-path propagation by Section II-D5;
- 20:       Superposition diffraction loss gain to free space model;
- 21:     **end if**
- 22:     **if**  $N = 2$  **then**
- 23:       Simplify mountains by Section II-D4;
- 24:       Jump to  $N = 1$ ;
- 25:     **end if**
- 26:     **if**  $N = 3$  **then**
- 27:       Simplify mountains by Section II-D4;
- 28:       Jump to  $N = 1$ ;
- 29:     **end if**
- 30:     **if**  $N > 3$  **then**
- 31:       LongleyRice's  $\Delta h$  estimation PL by Section II-D4;
- 32:       Superposition loss gain to free space model;
- 33:     **end if**
- 34:   **end if**
- 35: **end function**
- 36:  $PL_{P2P} \leftarrow PL_{prop}$ .

---

### Algorithm 2 uRTAPM-P2A

---

**Input:**  $ter_{pa}, pro_{pa}, sig_{pa}, env_{pa}, con_{pa}$ ;  
**Output:** Target area PL  $PL_{P2A}$ .

- 1: Convert DEM grid to TIN grid via Section II-B;
- 2: Calculate the number of TIN grids as  $N_{TIN}$ ;
- 3: **for**  $i = 1 \rightarrow N_{TIN}$  **do**
- 4:    $PL_{P2A} \leftarrow uRTAPM - P2P(ter_{pa}, pro_{pa}, sig_{pa}, env_{pa}, con_{pa})$ ;
- 5: **end for**
- 6: Display  $PL_{P2A}$  on the TIN grid.

---

## III. EXPERIMENTAL

To evaluate the feasibility and reliability of the method in Section II, simulation and actual measurement verification are necessary. The following are all implemented on the MATLAB

Table II  
PARAMETER DESCRIPTION

Parameters	Values
Frequency	900 MHz
Transmitter antenna height $h_t$ (relative to the ground)	15 m
Receiver antenna height $h_r$ (relative to the ground)	1.50 m
Polarization mode	horizontal
Antenna type	omnidirectional
Surface relative permittivity	$25 \text{ S.m}^{-1}$
Surface conductivity	$0.02 \text{ S.m}^{-1}$
Surface refractivity	301 N-units
$timepct$	0.90
$locpct$	0.90
$conpct$	0.90

computing platform.

### A. Environment and Simulation

Longling County, located in the border area of Yunnan, China, was one of the main battlefields in Western Yunnan during the Second World War. The Songsan Battlefield Site, which is 22 km east of Longling County, is a famous local tourist attraction. The area is a typical rural environment with extremely rugged terrains. Eighty-five percent of the ground is covered by broad-leaved forests approximately 20 meters high with bare rocks or overgrown weeds on steep slopes. Affected by the subtropical climate and lush vegetation, the region is humid and foggy all year round. In particular, the target area is characterized by steep mountains and alternates between peaks and valleys in the north and south with a very typical natural geographical vertical belt landscape of alpine valleys. The peak of this area is 2400 m above sea level, and the canyon altitude is only 500 m. According to Sections II-A and II-B, this area is visualized in 3D, and the TIN grid is filled with elevation values, as shown in Fig. 6 (a).

1) *uRTAPM-P2P Simulation*: uRTAPM-P2P is implemented by Algorithm 1, which is expressed in Section II-D6. The transmitter coordinates are (24.6945, 98.7898), and the receiver coordinates are (24.6724, 99.0806), as shown in Tx and Rx, respectively, in Fig. 6 (a). The other parameters are shown in Table II. Fig. 6 (b) shows the Tx-to-Rx terrain profile data (right vertical axis) and the corresponding PL prediction value (left vertical axis) with different propagation distances (horizontal axis). In terms of transmitter location, the terrain is tricky due to the half near distances are high terrain and the half far away with low terrain. The simulation shows that compared to the low-altitude terrain below TX, the high-altitude terrain above Tx more greatly affects the PL and shows a more dramatic fluctuation in the PL curve. In any case, the obstruction of radio waves by ridges or hilltops is obvious.

2) *uRTAPM-P2A Simulation*: The uRTAPM-P2A is implemented by Algorithm 2, which is expressed in Section II-D6. First, Algorithm 1 is invoked to calculate  $PL_{P2P}$  from the transmitter to the center of each TIN grid. Then, the program traverses the entire target area and fills the predicted loss values into the TIN grid. The transmitter coordinates are (24.7014, 98.8802), and the receiver coordinates are the center of the TIN grid. The other parameters are shown in Table II.

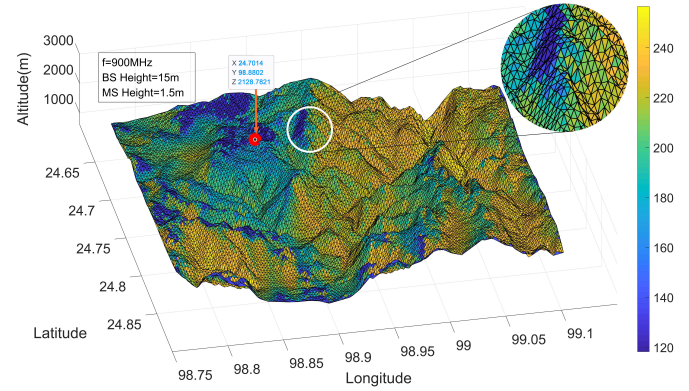


Fig. 7. uRTAPM-P2A simulation. PL prediction results of uRTAPM-P2A in Songshan, Yunnan, China (longitude: 98.7643 to 99.1129, latitude: 24.6474 to 24.8613); the color bar on the right shows the PL prediction value in dB.

The PL coverage of the transmitter (Tx) in the target area is shown in Fig. 7. This figure shows that the terrain greatly influences radio waves, and the distribution of PL in this area is extremely uneven, thus also leading to difficulty in achieving effective network planning and optimization in the uRTA.

### B. Measurement and Verification

Although the simulation in Section III-A intuitively shows the extreme effect of terrain on radio waves, to further evaluate the prediction accuracy and the details that the simulation may ignore, the PL prediction value should be compared with the measured value. As described in our previous work [10], this paper realizes the measurement scheme through the Huawei E392u-92 terminal, global positioning system (GPS) receiver, GENEX Probe V300R005C00SPC700 software, ENNX Assistant V300R005C00SPC700 software, SignalTEMMap software, and personal computer (PC). Here,  $h_t$  is 15 m,  $h_r$  is 1.5 m, the antenna radiation power is 45.4 dBm, the center frequency is 900 MHz, the bandwidth is 12 MHz, the antenna gain is 11 dBi, the antenna type is omnidirectional, and the sum loss of the feeder and vehicle body is 10 dB. In this paper, BS-1, BS-2 and BS-3 were tested with coordinates of (24.7033, 98.9001), (24.7391, 98.9050), and (24.7207, 98.8983), respectively. The receiver field strength value and GPS record value are displayed on Google Earth, as shown in Figs. 8 (a), 9 (a), and 10 (a).

Comparisons of the measured values of radio wave PL of BS-1, BS-2, and BS-3 with the predicted values of each model (ITM-LongleyRice, Okumura-Hata, COST-231, SPM, and uRTAPM) with logarithmic coordinates are shown in Figs. 8(b), 9 (b), and 10 (b), respectively. Here, the symbol “\*” denotes the measured value, and the other symbols show the predicted value of the corresponding model. Due to the terrain and the test routes, overlapping test points in these figures mean the loss values with the same propagation distance at different locations. The rural environmental loss coefficients of the Okumura-Hata model, COST-231 model, and SPM can be found in [10]. In Figs. 8 (b), 9 (b), and 10 (b), the uRTAPM (our model) and ITM-LongleyRice (the baseline model) reflect the influence of terrain details on PL. In particular, in Fig. 8

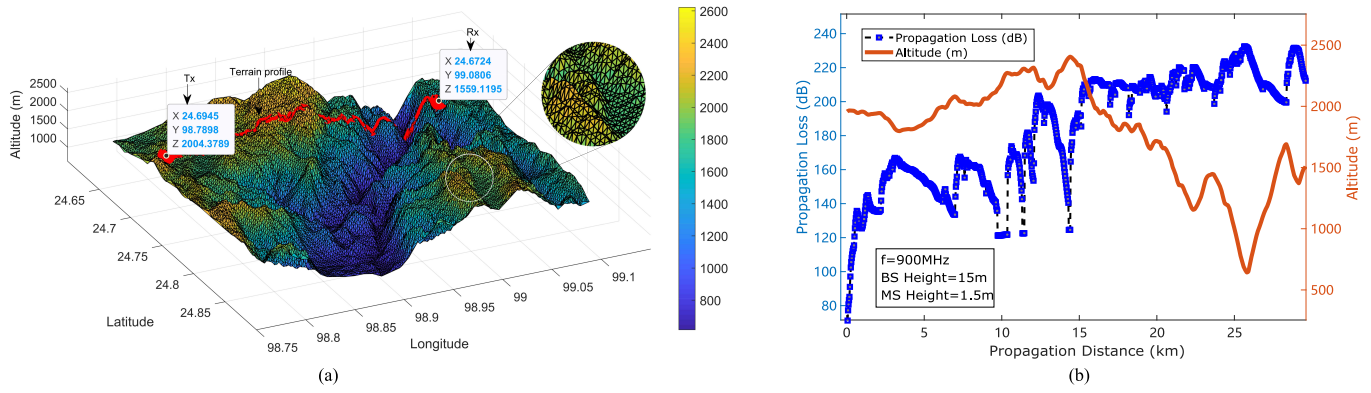


Fig. 6. uRTAPM-P2P simulation. (a) TIN grid 3D visualization in Songshan, Yunnan, China (longitude: 98.7643 to 99.1129, latitude: 24.6474 to 24.8613); the color bar on the right shows the altitude in meters. (b) uRTAPM-P2P PL prediction values and terrain profile data.

(b), the PL should generally increase with increasing propagation distance (positive linear correlation), but due to the influence of the terrain, this is not the case (negative linear correlation, see the PCC values in Table III). Fortunately, the uRTAPM and ITM-LongleyRice model still correctly predict the trend, and the uRTAPM considers the factors of multi-path propagation and local scattering caused by multi-mountains, thereby bringing the predicted fluctuation trend closer to the measured value. However, other commonly used PMs cannot predict the details of fading caused by terrain, mainly because the commonly used PMs do not consider terrain or only use an equivalent averaging method to estimate the degree of terrain fluctuation, which is not desirable in uRTAs.

To better compare between prediction models and measurements, first order statistics and correlation coefficient have been used [38].

Regarding first order statistics, we used the mean absolute error (MAE), root mean square error (RMSE), and standard deviation (SD). The related formulations are defined as follows:

$$MAE = \frac{1}{Nu} \sum_{i=1}^{Nu} X(i), \quad (10)$$

$$RMSE = \sqrt{\frac{1}{Nu} \sum_{i=1}^{Nu} X^2(i)}, \quad (11)$$

$$SD = \sqrt{\frac{1}{Nu} \sum_{i=1}^{Nu} |X(i) - MAE|^2}, \quad (12)$$

where  $X(i) = |PL_m(i) - PL_p(i)|$ ,  $PL_m(i)$  is the measured PL value,  $PL_p(i)$  is the predicted PL value, and  $Nu$  is the number of measured samples. Generally, the smaller these parameters are, the closer the predicted values are to the actual propagation.

The Pearson correlation coefficient (PCC) provides a measure of the degree of linear relationship between measured and predicted variables and is calculated as

$$PCC = \frac{\sum_{i=1}^{Nu} P_m P_p}{\sqrt{\sum_{i=1}^{Nu} (P_m)^2} \sqrt{\sum_{i=1}^{Nu} (P_p)^2}}, \quad (13)$$

where  $P_m = PL_m(i) - \overline{PL}_m$ ,  $P_p = PL_p(i) - \overline{PL}_p$ ; and  $\overline{PL}_m$  and  $\overline{PL}_p$  are the means of the measured and predicted values,

Table III  
MAE, RMSE, AND SD VALUES WITH BS-1

Model	MAE (dB)	RMSE (dB)	SD (dB)	PCC (dB)
ITM-LongleyRice	19.61	20.39	8.58	0.86
Okumura-Hata	28.43	31.25	12.95	-0.75
COST-231	30.79	33.41	12.95	-0.75
SPM	17.63	20.77	10.97	-0.75
uRTAPM	1.62	18.50	8.19	0.92

Table IV  
MAE, RMSE, AND SD VALUES WITH BS-2

Model	MAE (dB)	RMSE (dB)	SD (dB)	PCC (dB)
ITM-LongleyRice	15.42	35.68	14.36	0.74
Okumura-Hata	41.51	42.02	17.24	0.46
COST-231	43.87	44.36	17.24	0.46
SPM	29.30	39.97	16.98	0.46
uRTAPM	7.08	22.68	11.51	0.89

respectively. The PCC has a value between +1 and -1. A value of +1 is total positive linear correlation, 0 is no linear correlation, and -1 is total negative linear correlation.

The MAE, RMSE, SD, and PCC of the predicted values of each model and the measured values are shown in Tables III, IV, and V for BS-1, BS-2, and BS-3, respectively. All these tables show that compared with the other models, the uRTAPM has smaller MAE, RMSE, and SD values and a stronger linear correlation with the measured values.

Table V  
MAE, RMSE, AND SD VALUES WITH BS-3

Model	MAE (dB)	RMSE (dB)	SD (dB)	PCC (dB)
ITM-LongleyRice	28.39	37.65	13.62	0.72
Okumura-Hata	43.53	44.83	11.05	0.51
COST-231	45.89	47.13	11.31	0.51
SPM	31.32	33.06	10.44	0.51
uRTAPM	25.52	27.83	9.23	0.82

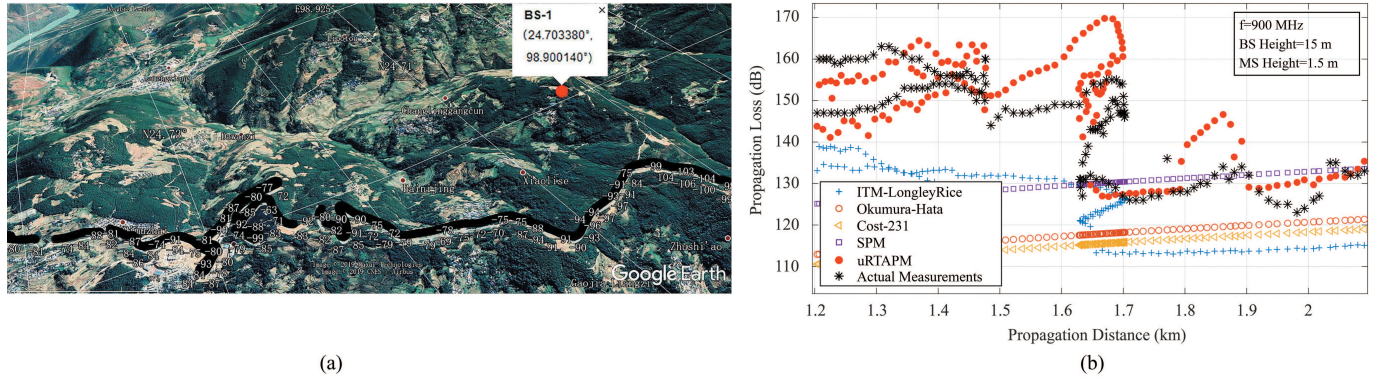


Fig. 8. BS-1 measurement. (a) The receiver field strength values and the GPS record values are displayed on Google Earth. (b) The commonly used PM prediction values are compared with the measured values.

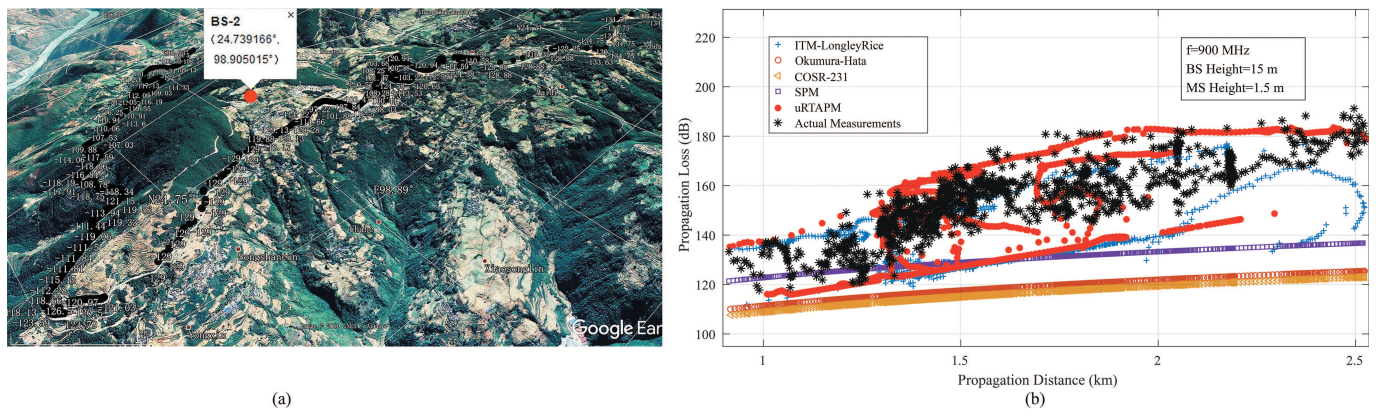


Fig. 9. BS-2 measurement. (a) The receiver field strength values and the GPS record values are displayed on Google Earth. (b) The commonly used PM prediction values are compared with the measured values.

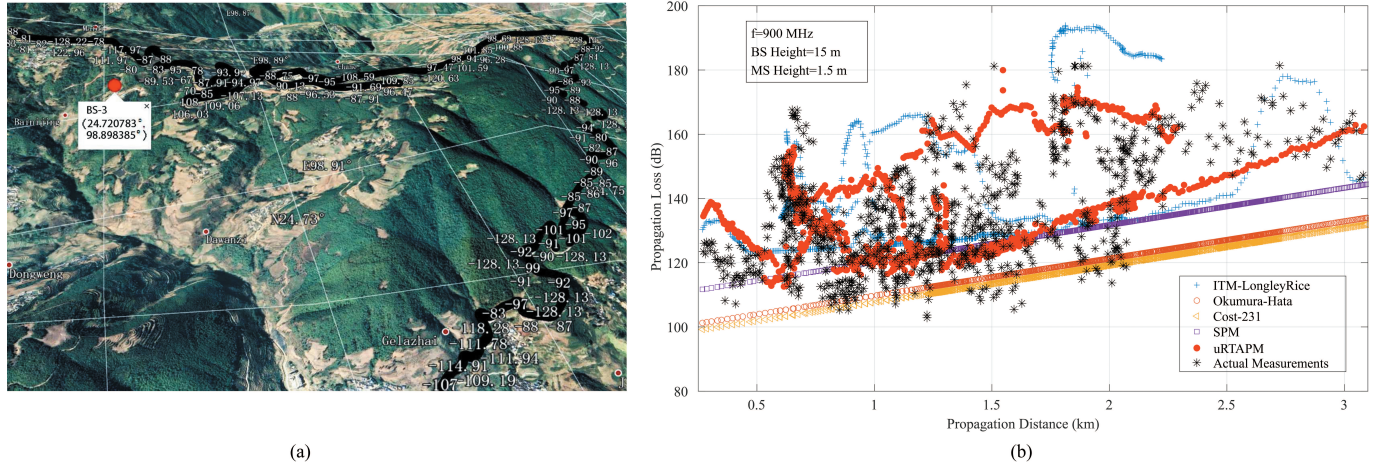


Fig. 10. BS-3 measurement. (a) The receiver field strength values and the GPS record values are displayed on Google Earth. (b) The commonly used PM prediction values are compared with the measured values.

### C. Runtime and Analysis

To characterize the running time, the Intel(R) Core(TM) i5-8500 central processing unit (CPU) @3.00 Ghz, x64 processor, Windows 10 operating system, and R2019b Update 3(9.7.0.1261785) MATLAB computing platform are used. In a certain simulation, the average calculation time of each P2P loss is shown in Table VI. In Table VI, the Okumura-Hata [10],

COST-231 [11], and SPM [12] algorithm inputs include only the frequency, effective height of the transceiver, and propagation distance. Because these algorithms are analytically formulated, the calculation time is shorter, but the prediction results are not sensitive to the terrain, and the prediction accuracy is worse. The ITM-LongleyRice model was used to calculate the terrain profile data and the parameters shown in

Table VI  
COMPARISON OF RUN TIMES (P2P) BETWEEN ALGORITHMS

Model	Run time (s)	Model	Run time (s)
ITM-LongleyRice	0.13	SPM	$0.17 \times 10^{-2}$
Okumura-Hata	$0.22 \times 10^{-2}$	uRTAPM	0.46
COST-231	$0.29 \times 10^{-2}$		

Table II; the resulted was a long running time and improved prediction accuracy. However, multi-path and multi-obstacle diffraction behaviors are not considered. Our uRTAPM algorithm overcomes the shortcomings of the aforementioned algorithms and focuses on the prediction of PL in extremely rugged regions with the longest running time and the highest accuracy. Generally, the running time is strongly related to the irregularity of the terrain and the sampling accuracy of the terrain data.

#### IV. DISCUSSION

The previous section shows the implementation of the uRTAPM and is used to predict the PL in the uRTAs. Both simulation and actual measurements show that our method exhibits more details of the PL caused by terrain and performs better than other models. The uRTAPM focuses on the following improvements: (i) The specific path parameters are always known when  $N \leq 3$ ; thus, the shortcomings of the ITM-LongleyRice model in assessing the regional coverage according to only  $\Delta h$  are improved; (ii) the TIN method can improve the accuracy of surface coverage in the uRTAPM-P2A model and is more effective in portraying ridges and canyons; (iii) in contrast to the ITM-LongleyRice model, this paper considers multi-mountain propagation and multi-path propagation.

It should be emphasized that the real mobile communication scene is usually within a few kilometers, e.g., 2.5 km, as shown in Fig. 9 (b). In the simulation section (i.e., Section III-A) of this paper, to thoroughly demonstrate the influence of terrain on PL, the simulation range is intentionally expanded, e.g., to 30 km, as shown in Fig. 6 (b). In addition, some limitations are noteworthy. In Section II-D5, a small mountain size, (that is,  $|x_j - x_i|$  is small), indicates that the diffraction clearance is small. To improve the calculation efficiency, the intersection point of  $|x_j - x_i| < 100$  m is not considered in this paper. In addition, the influence of  $h_1$  or  $h_2$  on the diffraction is neglected when the two sides of the mountain extend farther; i.e., when  $h_1$  or  $h_2$  is large ( $> 2h_0$ ), as assumed by the knife-edge diffraction model.

In addition, is it feasible to superimpose multipath diffraction components generated by obstacles with limited width? The answer is yes. According to J. Kunisch *et al.* [18], the diffraction gain caused by a stripe is regarded as the diffraction loss produced by two knife-edge models. Subsequently, in [19], [20], [39], and [37], the diffraction loss of the human body on radio waves is equivalent to the sum of the losses formed by three knife-edge models. In particular, the International Telecommunication Unions (ITU's) recommendations (ITU-R P.526-15) for diffraction modeling of finite-width

obstacles are a summary of this approach; see page 30, Eqs. (26)-(29) and Eq. (67) in [36]. In the aforementioned works, for example, [19] and [20], the movement characteristics of obstacles are considered in a dynamic environment, so  $e^{(-2\pi f t)}$  is multiplied by the diffraction gain of each multipath component to correct the phase. However, the environment we consider is a time-invariant flat fading and does not focus on the receiver's mobile characteristics, so this correction term is not used, as shown in [37]. In summary, the cone model can be used to estimate the PL in the uRTAs, and the actual measurement also implies that this method is more accurate than current state-of-the-art methods.

In practical engineering, an MAE close to 0 dB and an SD less than 15 dB indicate an ideal estimation result in a typical rural environment [40]. As Tables III-V imply, our approach can be optimized. We eventually plan to improve our method in the following aspects: (i) The uRTAPM needs to be tuned by many actual measurement data (more frequencies and more terrain). The goal of tuning is to make the MAE, RMSE, and SD values converge as quickly as possible to the minimum. Based on the uRTAPM, the parameters that can be corrected include surface relative permittivity, surface conductivity, surface refractivity, and DEM data accuracy, which are related to vegetation coverage, surface clutter, computational efficiency, and so on. (ii) Optimizing the calculation method of the uRTAPM. Figs. 8 (b), 9 (b), and 10 (b) show that the uRTAPM is more sensitive than the ITM-LongleyRice model to terrain possibly mainly because the local scattering loss gain is superimposed due to multi-path and multi-mountain methods in the uRTAPM, and the influence weight of this propagation type can be appropriately reduced. (iii) Other details. For example, one-day or seasonal temperature differences and rain attenuation can also be considered. In particular, when the frequency band is greater than 6 GHz, the weight of rain attenuation is increased. In addition, this paper is based on the omnidirectional single antenna for calculation. We eventually plan to consider the directional antenna mode, multiple-input multiple-output antenna, beamforming, azimuth of arrival (delay, phase), and other factors. Currently, with the popularity of machine learning algorithms, such as neural networks, the study of PL prediction based on machine learning has attracted the attention of researchers [41], [42]. This method needs to collect an extensive dataset related to a specific environment and then train the data with a machine learning algorithm to generate a prediction model. However, due to the special topography, obtaining many accurately labeled measurement data is not easy [43], and how to map the classification of obstacles to PL is also an open question. Nevertheless, in uRTAs, using drones for measurement and using machine learning algorithms for parameter correction are one possible future research direction.

Some practical implications of this study include the following:

- 1) At present, the commonly used method of radio wave PL prediction is to use existing empirical PMs or to modify them to obtain the propagation characteristic estimates of specific areas. These methods all rely heavily on test data for specific environments and have weak environmental

adaptability. However, the uRTAPM organically combines empirical PMs, actual terrain data, and geometric propagation theories and selects or improves classical PMs that have been proven to be effective by many experiments to perform PL prediction based on actual conditions. Even without a sufficient test cost or limited test conditions (e.g., the road test route does not exist, or the test equipment cannot be installed), the uRTAPM method can still provide an important reference for radio wave PL prediction in complex terrain environments.

- 2) Compared with empirical PMs (e.g., the Okumura-Hata model) that are based only on statistical data of specific propagation environments, the uRTAPM can reflect the details of fading due to terrain, thereby greatly improving PL prediction accuracy with respect to uRTAs. In particular, our proposed cone model upgrades a two-dimensional scene to a three-dimensional scene and has obvious advantages in considering multipath propagation, which is ignored by traditional non-ray-tracing PMs.
- 3) Compared with the deterministic PM based on ray-tracing, the uRTAPM greatly reduces computational complexity in evaluating the effect of obstacles on losses. Because the former attempts to consider all possible rays from the transmitter to the receiver, the complexity of this model increases exponentially as the accuracy of the 3D map, the number of rays, and the order of reflection increase [44]. However, the uRTAPM focuses only on the main secondary Huygens source location on the obstacle, thereby reducing computational complexity and retaining prediction accuracy. In addition, with a certain terrain data accuracy, due to the discreteness of the sampling points, we can always calculate the secondary Huygens source position at the edge of the obstacle, thereby protecting the algorithm from deadlock, e.g., point  $(x_k, y_k)$  in Fig. 5. However, the ray-tracing method is not as capable in dealing with circular contour obstacles and complex terrain environments [45]. Therefore, the uRTAPM is attractive in terms of accuracy and complexity. The uRTAPM method is also expected to be extended to the impact of urban buildings on PL.
- 4) In this research, for the first time, DEM data, TIN segmentation techniques, classic PMs, and cone models were synthesized. We focused mainly on the prediction of PL for uRTAs with  $\Delta h > 1000$  m and carried out actual test verification. To the authors' best knowledge, until this paper, there has been no published data to fully support uRTA radio PL prediction.

## V. CONCLUSION

In uRTAs with  $\Delta h > 1000$  m, the existing PM cannot meet the requirements of radio field strength prediction accuracy. This paper focuses on the influence of terrain on radio wave PL, and implements a method for predicting PL in uRTAs, namely, the uRTAPM. Compared with current commonly used PMs, such as the ITM-LongleyRice model, the Okumura-Hata model, the COST-231 model, and the SPM, the simulations show that both uRTAPM-P2P and uRTAPM-P2A suitably

demonstrate the effect of terrain on radio waves, and actual measurements confirm that the uRTAPM model is more effective than the other models. Concerning uRTAs, this research is expected to be used for fine-grained network planning and optimization, which may include automatic driving, the Internet of things, FM radio, TV broadcasting, and emergency communications.

## APPENDIX A CALCULATE THE DIFFRACTION PARAMETERS OF EACH KNIFE-EDGE MODEL

In Fig. 5, the dimensions are defined as follows:  $d_{F1} \stackrel{\text{def}}{=} \overline{TO'}$ ;  $d_{F2} \stackrel{\text{def}}{=} \overline{O'R}$ ;  $d_{S1} \stackrel{\text{def}}{=} \overline{TC'}$ ;  $d_{S2} \stackrel{\text{def}}{=} \overline{C'R}$ ;  $d_{T1} \stackrel{\text{def}}{=} \overline{TD'}$ ;  $d_{T2} \stackrel{\text{def}}{=} \overline{DR}$ ;  $d_1 \stackrel{\text{def}}{=} \overline{TO}$ ;  $d_2 \stackrel{\text{def}}{=} \overline{OR}$ ;  $d \stackrel{\text{def}}{=} \overline{TR}$ ;  $h_0 \stackrel{\text{def}}{=} \overline{OO'}$ ;  $h_1 \stackrel{\text{def}}{=} \overline{CC'}$ ;  $h_2 \stackrel{\text{def}}{=} \overline{DD'}$ . In these definitions,  $d_F$ ,  $d_S$  and  $d_T$  represent the diffraction paths of the First, Second, and Third paths, respectively. Further,  $h_0$ ,  $h_1$ , and  $h_2$  denote the effective Fresnel clearances of the first, second, and third paths respectively, which are the vertical distances from point  $O$ , point  $C$ , and point  $D$  to the  $L-O-S$ . Then, the difference between the diffracted path and the direct path can be obtained from the geometry of Fig. 5 as

$$\Delta_\omega = d_\omega - d = \underbrace{\sqrt{d_1^2 + h_\mu^2}}_{d_{\omega_1}, \text{ source-to-edge}} + \underbrace{\sqrt{d_2^2 + h_\mu^2}}_{d_{\omega_2}, \text{ edge-to-observation}} - \underbrace{(d_1 + d_2)}_{d, \text{ LOS path}}, \quad (14)$$

where,

$$\omega, \mu = \begin{cases} \omega = F, \mu = 0 & \text{with first path;} \\ \omega = S, \mu = 1 & \text{with second path;} \\ \omega = T, \mu = 2 & \text{with third path.} \end{cases} \quad (15)$$

Equation (14) can be approximated as

$$\Delta_\omega \approx d_1 \left( 1 + \frac{h_\mu}{2d_1^2} \right) + d_2 \left( 1 + \frac{h_\mu}{2d_2^2} \right) - (d_1 + d_2) = \frac{h_\mu^2}{2} \left( \frac{1}{d_1} + \frac{1}{d_2} \right), \quad (16)$$

the corresponding phase difference is given by

$$\frac{2\pi\Delta_\omega}{\lambda} = \frac{2\pi}{\lambda} \frac{h_\mu^2}{2} \left( \frac{1}{d_1} + \frac{1}{d_2} \right). \quad (17)$$

According to Section II-C3, Eq. (17) is often normalized using the dimensionless Fresnel-Kirchhoff diffraction parameter  $v$ , which is given by

$$v_\omega \stackrel{\text{def}}{=} h_\mu \sqrt{\frac{2}{\lambda} \left( \frac{1}{d_1} + \frac{1}{d_2} \right)}. \quad (18)$$

Collecting the  $h_\mu$  value from Section II-D5 produces a set of  $v_\omega$  values as a function of Eq. (7) that results in a constant-amplitude electric field at the receiver location.

## REFERENCES

- [1] L. Li, Z. S. Wu, L. K. Lin, R. Zhang, and Z. W. Zhao, "Study on the prediction of troposcatter transmission loss," *IEEE Transactions on Antennas and Propagation*, vol. 64, no. 3, pp. 1071–1079, 2016.
- [2] Z. Yun and M. F. Iskander, "Ray tracing for radio propagation modeling: Principles and applications," *IEEE Access*, vol. 3, pp. 1089–1100, 2015.
- [3] K.-W. Kim and S.-J. Oh, "Geometric optics-based propagation prediction model in urban street canyon environments," *IEEE Antennas and Wireless Propagation Letters*, vol. 15, pp. 1128–1131, 2015.
- [4] Z. He, T. Su, H. Yin, and R. Chen, "Wave propagation modeling of tunnels in complex meteorological environments with parabolic equation," *IEEE Transactions on Antennas and Propagation*, vol. 66, no. 12, pp. 6629–6634, 2018.
- [5] G. A. Hufford, A. G. Longley, and W. A. Kissick, "A guide to the use of its irregular terrain model in the area prediction mode," vol. 83, no. 4, pp. 1–117, 1982.
- [6] M. A. Silva, E. Costa, and M. Liniger, "Analysis of the effects of irregular terrain on radio wave propagation based on a three-dimensional parabolic equation," *IEEE transactions on antennas and propagation*, vol. 60, no. 4, pp. 2138–2143, 2012.
- [7] Q. Guo and Y. Long, "Pade second-order parabolic equation modeling for propagation over irregular terrain," *IEEE Antennas and Wireless Propagation Letters*, vol. 16, pp. 2852–2855, 2017.
- [8] C. Phillips, D. Sicker, and D. Grunwald, "A survey of wireless path loss prediction and coverage mapping methods," *IEEE Communications Surveys & Tutorials*, vol. 15, no. 1, pp. 255–270, 2012.
- [9] A. A. Khuwaja, Y. Chen, N. Zhao, M.-S. Alouini, and P. Dobbins, "A survey of channel modeling for uav communications," *IEEE Communications Surveys & Tutorials*, vol. 20, no. 4, pp. 2804–2821, 2018.
- [10] H. Li, X. He, and W. He, "Review of wireless personal communications radio propagation models in high altitude mountainous areas at 2.6 ghz," *Wireless Personal Communications: An International Journal*, vol. 101, no. 2, pp. 735–753, 2018.
- [11] A. Hikmaturohman, S. Larasati, and E. S. Nugraha, "Analysis cost 231 multiwall model on 4g lte fdd 1800 and 900 mhz femtocell network planning," *JAICT*, vol. 1, no. 1, pp. 1–7, 2016.
- [12] S. I. Popoola, A. A. Atayero, N. Faruk, C. T. Calafate, L. A. Olawoyin, and V. O. Matthews, "Standard propagation model tuning for path loss predictions in built-up environments," in *International Conference on Computational Science and Its Applications*. Springer, 2017, pp. 363–375.
- [13] L. Santos Vasconcelos and G. Arantes Carrijo, "A new correction for bullington multiple knife-edge model in vhf and uhf tv bands," *IEEE Latin America Transactions*, vol. 14, no. 12, pp. 4646–4651, 2016.
- [14] W. Samuel, F. O. C. Nwaduwa, and T. C. Oguichen, "Algorithm for computing n knife edge diffraction loss using epstein-peterson method," *American Journal of Software Engineering and Applications*, vol. 6, no. 2, pp. 40–43, 2017.
- [15] Y. Song and A. Akgolu, "Parallel implementation of the irregular terrain model (itm) for radio transmission loss prediction using gpu and cell be processors," *IEEE Transactions on Parallel and Distributed Systems*, vol. 22, no. 8, pp. 1276–1283, 2011.
- [16] J. S. Tietjen, "Anita longley's legacy: The longley-rice model - still going strong after almost 50 years," *IEEE Antennas and Propagation Magazine*, vol. 55, no. 3, pp. 237–240, 2013.
- [17] M. Vuckovik, D. Trajanov, and S. Filiposka, "Durkin's propagation model based on triangular irregular network terrain," in *International Conference on ICT Innovations*. Springer, 2011, pp. 333–341.
- [18] J. Kunisch and J. Pamp, "Ultra-wideband double vertical knife-edge model for obstruction of a ray by a person," in *2008 IEEE International Conference on Ultra-Wideband*, vol. 2. IEEE, 2008, pp. 17–20.
- [19] T. Wang, M. Umehira, H. Otsu, S. Takeda, T. Miyajima, and K. Kagoshima, "A twin cylinder model for moving human body shadowing in 60ghz wlan," in *2015 21st Asia-Pacific Conference on Communications (APCC)*. IEEE, 2015, pp. 188–192.
- [20] U. T. Virk and K. Haneda, "Modeling human blockage at 5g millimeter-wave frequencies," *IEEE Transactions on Antennas and Propagation*, vol. 68, no. 3, pp. 2256–2266, 2019.
- [21] Y. Dalveren, A. H. Alabish, and A. Kara, "A simplified model for characterizing the effects of scattering objects and human body blocking indoor links at 28 ghz," *IEEE Access*, vol. 7, pp. 69 687–69 691, 2019.
- [22] J. S. Lu, H. L. Bertoni, K. A. Remley, W. F. Young, and J. Ladbury, "Site-specific models of the received power for radio communication in urban street canyons," *IEEE Transactions on Antennas and Propagation*, vol. 62, no. 4, pp. 2192–2200, 2014.
- [23] X. Zhao, H. Zhang, S. Geng, K. Haneda, J. Meinila, and T. Jamsa, "A novel full path-loss model for a street crossing in urban microcells," *IEEE Transactions on Antennas & Propagation*, vol. 63, no. 12, pp. 5878–5883, 2015.
- [24] S.-S. Oh and Choi, "An empirical propagation prediction model for urban street canyon environments at 6, 10, and 18 ghz," *Microwave and Optical Technology Letters*, vol. 61, no. 6, pp. 1574–1578, 2019.
- [25] J. H. Jung, J. Lee, J. H. Lee, Y. H. Kim, and S. C. Kim, "Ray-tracing-aided modeling of user-shadowing effects in indoor wireless channels," *IEEE Transactions on Antennas and Propagation*, vol. 62, no. 6, pp. 3412–3416, 2014.
- [26] G. Steinbock, T. Pedersen, B. H. Fleury, W. Wang, and R. Raulefs, "Experimental validation of the reverberation effect in room electromagnetics," *IEEE Transactions on Antennas & Propagation*, vol. 63, no. 5, pp. 2041–2053, 2015.
- [27] J. Jarvelainen, K. Haneda, and A. Karttunen, "Indoor propagation channel simulations at 60 ghz using point cloud data," *IEEE Transactions on Antennas & Propagation*, vol. 64, no. 10, pp. 4457–4467, 2016.
- [28] A. I. Sulyman, A. Alwarafy, G. R. Maccartney, T. S. Rappaport, and A. Al-Sanie, "Directional radio propagation path loss models for millimeter-wave wireless networks in the 28, 60, and 73 ghz bands," *IEEE Transactions on Wireless Communications*, vol. 15, no. 10, pp. 6939–6947, 2016.
- [29] J. Zang and X. Wang, "Measurements and modeling of path loss over irregular terrain for near-ground and short-range communications," *Progress In Electromagnetics Research*, vol. 57, pp. 55–62, 2017.
- [30] J. Hejselbæk, J. Ø. Nielsen, W. Fan, and G. F. Pedersen, "Empirical study of near ground propagation in forest terrain for internet-of-things type device-to-device communication," *Ieee Access*, vol. 6, pp. 54 052–54 063, 2018.
- [31] G. Apaydin and L. Sevgi, "Numerical investigations of and path loss predictions for surface wave propagation over sea paths including hilly island transitions," *IEEE Transactions on Antennas & Propagation*, vol. 58, no. 4, pp. 1302–1314, 2010.
- [32] J. R. Shewchuk, "Delaunay refinement algorithms for triangular mesh generation," *Computational geometry*, vol. 22, no. 1-3, pp. 21–74, 2002.
- [33] H. Liu and C. Wu, "Developing a scene-based triangulated irregular network (tin) technique for individual tree crown reconstruction with lidar data," *Forests*, vol. 11, pp. 1–28, 2019.
- [34] A. F. Molisch, *Wireless communications*. John Wiley & Sons, 2011.
- [35] W. C. Y. Lee, *Mobile Communications Engineering: Theory and Applications*. New York: MacGraw-Hill, 1982.
- [36] ITU. (2019) Itu-r p.526-15 propagation by diffraction. [Online]. Available: [https://www.itu.int/dms\\_pubrec/itu-r/rec/p/R-REC-P.526-15-201910-1.pdf](https://www.itu.int/dms_pubrec/itu-r/rec/p/R-REC-P.526-15-201910-1/P.526-15-201910-1.pdf)
- [37] J. Medbo and F. Harrysson, "Channel modeling for the stationary ue scenario," in *2013 7th European Conference on Antennas and Propagation (EuCAP)*. IEEE, 2013, pp. 2811–2815.
- [38] N. Cota, A. Serrador, P. Vieira, A. R. Beire, and A. Rodrigues, "On the use of okumurahata propagation model on railway communications," *Wireless Personal Communications*, vol. 93, no. 3, pp. 725–736, 2017.
- [39] M. Cheffena, "Physical-statistical channel model for signal effect by moving human bodies," *EURASIP Journal on Wireless Communications and Networking*, vol. 2012, no. 1–13, p. 77, 2012.
- [40] R. C. V. Macario, "The mobile radio propagation channel," *Iee Review*, vol. 38, no. 6, p. 234, 1992.
- [41] M. Ayadi, A. B. Zineb, and S. Tabbane, "A uhf path loss model using learning machine for heterogeneous networks," *IEEE Transactions on Antennas and Propagation*, vol. 65, no. 7, pp. 3675–3683, 2017.
- [42] S. I. Popoola, E. Adetiba, A. A. Atayero, N. Faruk, and C. T. Calafate, "Optimal model for path loss predictions using feed-forward neural networks," *Cogent Engineering*, vol. 5, no. 1, pp. 1–19, 2018.
- [43] A. Al-Hourani and K. Gomez, "Modeling cellular-to-uav path-loss for suburban environments," *IEEE Wireless Communications Letters*, vol. 7, no. 1, pp. 82–85, 2017.
- [44] D. He, B. Ai, K. Guan, L. Wang, Z. Zhong, and T. Kürner, "The design and applications of high-performance ray-tracing simulation platform for 5g and beyond wireless communications: A tutorial," *IEEE Communications Surveys & Tutorials*, vol. 21, no. 1, pp. 10–27, 2018.
- [45] D. Green, Z. Yun, and M. F. Iskander, "Path loss characteristics in urban environments using ray-tracing methods," *IEEE Antennas and Wireless Propagation Letters*, vol. 16, pp. 3063–3066, 2017.



**Huafu Li** received the M.S. degree in radio physics from Yunnan Normal University, Kunming, China, in 2018. He is currently pursuing the Ph.D. degree with the School of Electronic and Information Engineering, Harbin Institute of Technology, Harbin, China. His research interests include wireless communication and propagation model.



**Wexxue He** received the B.S. degree in physics from Yunnan Normal University, Kunming, China, in 1987, the M.S. degree in electronic engineering from Xian Jiao Tong University, China, in 1990, and the Ph.D. degree in information and telecommunication from the University of Florence, Florence, Italy, in 1997. He is currently an associate professor with the department of Physics and Electronics, Yunnan Normal University, China. Prior to that, he ever worked with Nantian Corp., Huawei Ltd., UTStarcomm Corp., Guangdogn Weichuan Ltd., all in China. His current research interests include wireless communications, channel measurement, and machine learning.



**Xianguo He** received the B.S. degree in telecommunication engineering from Xian University of Posts & Telecommunications, Xian, China, in 2003, the M.S. degree in project management from Nanjing University of Posts & Telecommunications, Nanjing, China, in 2011. He is a senior engineer with China Mobile Corp., Yunnan Co., Ltd., Baoshan Branch, Baoshan, China, where he has been employed since 2011. His current research interests include mobile network plan & optimizing technology and industry management.